






REVIEW ARTICLE | JUNE 06 2025

Strain engineering of microfabricated diamond and its applications

Special Collection: [Ultrawide Bandgap Semiconductors](#)Wenjun Liang ; Limin Yang ; Jiaqi Zhu; Yiling Lian ; Yang Lu  

APL Mater. 13, 060602 (2025)

<https://doi.org/10.1063/5.0268185>

Articles You May Be Interested In

Hydrogel electronic materials and microfabrication processes for soft electronic applications

Appl. Phys. Rev. (July 2025)

Increased surface flashover voltage in microfabricated devices

Appl. Phys. Lett. (October 2013)

A superhigh-frequency optoelectromechanical system based on a slotted photonic crystal cavity

Appl. Phys. Lett. (November 2012)

APL Materials

Special Topics Open for Submissions

[Learn More](#)

Strain engineering of microfabricated diamond and its applications

Cite as: APL Mater. 13, 060602 (2025); doi: 10.1063/5.0268185

Submitted: 28 February 2025 • Accepted: 24 May 2025 •

Published Online: 6 June 2025



Wenjun Liang,¹  Limin Yang,²  Jiaqi Zhu,¹ Yiling Lian,¹  and Yang Lu^{1,3,a} 

AFFILIATIONS

¹ Department of Mechanical Engineering, The University of Hong Kong, Hong Kong, China

² Department of Mechanical Engineering, City University of Hong Kong, Hong Kong, China

³ Material Innovation Institute for Life Sciences and Energy, Shenzhen, China

Note: This paper is part of the Special Topic on Ultrawide Bandgap Semiconductors.

a) Author to whom correspondence should be addressed: yulu1@hku.hk

ABSTRACT

Diamond is considered the ultimate semiconductor material due to its excellent physical and electrical properties, such as ultrahigh thermal conductivity, ultrawide bandgap, and superhigh carrier mobility. After ultralarge deformation experimentally conducted on diamond in 2018 and 2021, strain engineering is a highly appealing candidate for tuning these properties of diamond, opening up potential applications in microelectronics and quantum technologies. In this review, we briefly review the implementation of strain engineering on diamond, including introducing dynamic strain by nanomechanical tests and maintaining static strain by various methods. We also provide a brief overview of the strain-induced property changes and the specific applications of the strained diamond.

© 2025 Author(s). All article content, except where otherwise noted, is licensed under a Creative Commons Attribution (CC BY) license (<https://creativecommons.org/licenses/by/4.0/>). <https://doi.org/10.1063/5.0268185>

I. INTRODUCTION

Diamond is widely recognized as a material with multidimensional excellent properties, such as ultrawide bandgap, extraordinary carrier mobility, and high thermal conductivity, making it regarded as the “ultimate semiconductor.” Due to the remarkable mechanical properties and chemical inertness of diamond, it faces challenges in terms of synthesis and processing. Over the past seven decades, the maximum size of single crystal diamond has reached ~4 in.,¹ and the smallest thickness of microfabricated diamond film has reached ~10 nm.² Diamond can be fabricated into two-dimensional pattern and three-dimensional structure, such as cantilever,^{3,4} ratchet,^{5,6} microdisk,^{7,8} and hemisphere,^{9,10} exhibiting its potential for micro-electromechanical systems (MEMS). These multiscale fabrication technologies form the cornerstone of diamond application in microelectronics,^{11–13} high-frequency power electronics,^{14–16} thermal management devices,^{17,18} and lithium metal batteries.^{19,20}

Strain engineering is a promising strategy to manipulate properties of materials, such as electronic, optical, and phononic properties.²¹ For silicon, strain engineering enables 15% improvement

of current drivability without any performance degradation,²² thermal conductivity can be reduced under inhomogeneous strain,²³ and quality factors can be increased.²⁴ For wide bandgap materials, such as silicon carbide (SiC) and gallium nitride (GaN), they have polarized covalent bonds compared to silicon, making them have different mechanisms and effects in strain engineering. For example, 2D SiC exhibits typical metallization in the special compression direction due to enhancement of the ionic character.²⁵ In addition, SiC and GaN also demonstrate a strong piezoelectricity effect, which does not exist in Si.^{26,27} Compared to SiC and GaN, diamond consists of non-polar covalent bonds and has a crystal structure similar to silicon. As an ultrawide bandgap material, the properties of diamond can be tuned by strain engineering as well, such as strain-induced metallization and improvement of thermal conductivity.^{28,29} The donor level of nitrogen in diamond can be shifted shallowed, unlocking new possibilities for diamond doping engineering, which is crucial for developing diamond-based semiconductor devices.^{30–32}

In this review, we highlight several aspects of strain engineering in diamond, including dynamic strain in diamond using nanomechanical test, static strain in diamond using non-mechanical test,

and manipulation of diamond properties using strain engineering. Furthermore, we also provide an overview of strained diamond applications in sensing and quantum technologies.

II. DYNAMIC STRAIN IN DIAMOND

Diamond is widely considered as the hardest material due to its ultrahigh covalent bond energy and atomic arrangement density. While the theoretical Young's modulus of diamond shows over 1000 gigapascals (GPa), bulk diamond exhibits representative brittleness and is not easy to be experimentally stretched or compressed elastically. Although diamond and its device fabrication witnessed a relatively systematic development, the elastic deformation of diamond and elastic-strain-induced properties modulation are just estimated from computational simulations yet remain empirically unverified, such as bandgap and thermal conductivity tuning.^{33,34} Nanomechanical test is a fundamental and quantitative method of studying mechanical properties of nanoscale materials, such as characterization of mechanics properties by testing one-dimensional nanowires and two-dimensional film.^{35–37} The current prevailing approaches for testing microfabricated diamond structures involve push-to-bend, tension, buckling, and compression using an *in situ* transmission electron microscope (TEM) and a scanning electron microscope (SEM) test.³⁸

An ultralarge (up to 9%) elastic deformation of diamond was demonstrated experimentally for the first time and analyzed by simulation in 2018.³⁹ Such ultralarge elastic deformation of diamond nanoneedle was completed through downward displacement of the diamond indenter tip. Owing to shape of the diamond indenter, a sideward displacement was induced after contacting the inclined surface of the indenter and, therefore, generated a push-to-bend deformation, as shown in Fig. 1(a1). Using SEM imaging, an ultralarge and fully reversible bending deformation of diamond nanoneedle was observed in a loading–unloading test, as shown in Fig. 1(a2). Using finite element method (FEM) simulation, it was found that the maximum local elastic strain was distributed on the tensile side of a bent diamond needle. The maximum stress was estimated at ~98 GPa, corresponding to the maximum tensile strain of 8.88%, as shown in Fig. 1(a3). Across two loading–unloading tests in the same diamond nanoneedle, the indenter downward displacement–load curves exhibited a close overlap between the first loading for elastic deformation (blue curve) and the reloading for final fracture (the red one), indicating the fully reversible elastic deformation of diamond nanoneedle, as shown in Fig. 1(a4). Following integrating systematic simulation and characterization, the essential conditions for realizing extremely high elastic strain of nanoscale diamond are a negligible number of defects and a comparatively smooth surface.

After the first observation of ultrahigh elastic strain in 2018, other researchers investigated methods to achieve and control elastic strain in microfabricated diamond structures.⁴⁰ To deeply investigate the factors for tunable elastic strain in diamond, they experimented on a series of microfabricated diamond nanoneedles with different crystal orientations and sizes using a compress-to-bend method.⁴¹ A representative loading–unloading process of *in situ* TEM loading test is shown in Fig. 1(b1). Using focused ion beam (FIB) milling and argon plasma thinning, a typical diamond needle sample was fabricated with a tip diameter of ~50 nm. Along the

axial direction, the diamond nanoneedle was buckled during a fabricated diamond indenter gradual downward motion. A super-large elastic buckling was approached and fully recovered after unloading. Using FEM simulation to reproduce the bent shape in Fig. 1(b1), the maximum tensile strain was estimated at ~10.1% on the tensile side and the maximum compressive strain approached ~11.4% on the compressive side of the diamond nanoneedle, as shown in Fig. 1(b2). For investigating lattice distortion, the selected area electron diffraction (SAED) pattern of the bent diamond needle located at the red circle in Fig. 1(c1) is shown in Fig. 1(c3). The initial d-spacing of (002) diamond lattice was measured ~1.70 Å before a compress-to-bending test. The value was increased to 1.94 Å when inducing a bent deformation in the diamond needle shown in Fig. 1(b1), implying that diamond (200) lattice is elongated ~9%, as shown in Fig. 1(b3). Using first-principle calculations, the theoretical stress–strain curves of uniaxial tension along different crystal orientations for bulk diamond were shown in Fig. 1(b4). The (100) direction diamond can theoretically approach higher tensile strain among three crystal directions, which was in agreement with the experimental tests. The experimental maximum stress value of the bending test of (100) diamond nanoneedles approached 125 GPa, reaching the Griffith theoretical strength of 122 GPa.

To generate uniform and controllable elastic strain in diamond, the uniaxial tension test is an effective strategy. A diamond bridge structure was fabricated by FIB, with a central beam length of 1 μm and width of 300 nm.⁴² The microfabricated diamond bridge structure was axially stretched through a fabricated diamond gripper, as shown in Fig. 1(c1). Along axial direction (diamond [101] direction), a series of elastic loading–unloading with gradient increase was applied to the diamond sample to study its reversible elastic deformation. By measuring the length between the fiducial markers at the two ends of the diamond central beam, the maximum value of elastic strain reached 7.5%, as shown in Fig. 1(c2). Using FEM simulation, the elastic strain was uniformly distributed along the axial direction inside the structure, with a maximum strain of ~9.1%. The electron diffraction pattern of the selected area along [001] zone axis revealed that the direction of loading aligns with [101] orientation, as shown in Fig. 1(c3). After three loading–unloading tests, the engineering stress–strain curves exhibited a high degree of proximity, indicating the fully reversible elastic deformation of diamond nanostructures. The slopes yielded a Young's modulus of ~865 GPa, closing the theoretical value of diamond along [101] direction, as shown in Fig. 1(c4). The uniaxial tension test can also be used to measure mechanical properties of two-dimensional materials, such as monolayer graphene and hexagonal boron nitride (h-BN).^{43,44}

Carrying a uniaxial compression test for bulk diamond is challenging due to the tight-binding sp^3 bond, which is widely regarded as the most stable bond in carbon materials. A large elastic compressive deformation is difficult to be detected in the diamond pillar exhibiting brittle fracture.⁴⁵ In 2017, amorphous diamond, which consisted of complete sp^3 bonding, was synthesized using the diamond anvil cells (DACs) system.⁴⁶ After that, amorphous carbon samples, which are composed of high-fraction sp^3 -bonded carbon (~94% sp^3 bonding), exhibited an ultralarge elastic compressive strain in 2021.⁴⁷ The amorphous carbons were synthesized via C_{60} fullerene, using a high pressure and high temperature (HPHT) method. The high-resolution transmission electron microscopy (HRTEM) image and SAED pattern of a 94%

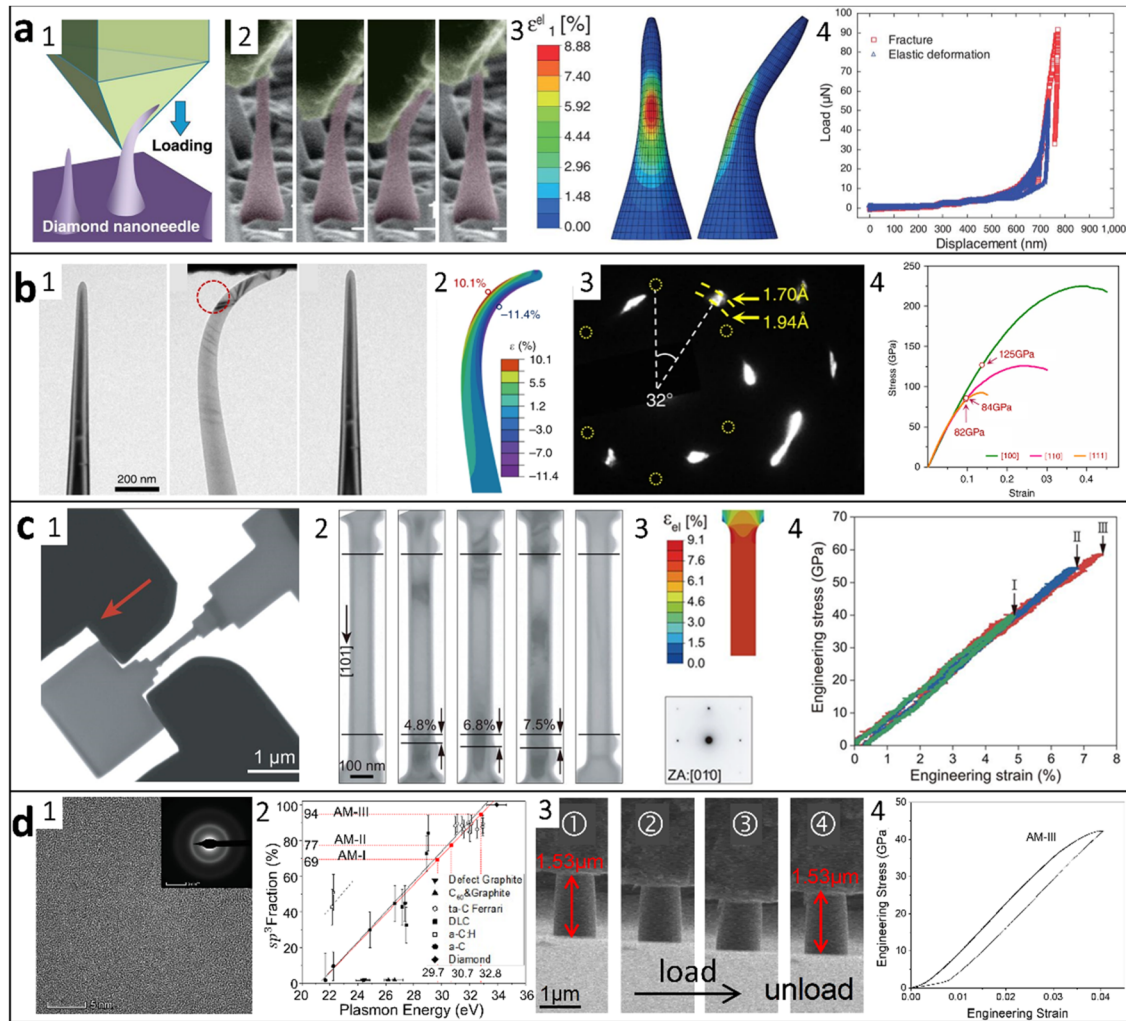


FIG. 1. Dynamic strain in diamond using an *in situ* mechanical test.³⁹ (a1) The schematic diagram of the *in situ* push-to-bend test of diamond nanoneedle (purple) using a diamond indenter (green). (a2) The representative images during the loading-unloading tests at panel (a1). (a3) FEM simulation result to reproduce the maximum bent deformation of the needle in panel (a2). (a4) The indenter downward displacement-load curves of two loading-unloading tests in the same diamond nanoneedle. The blue curve represents the recoverable elastic deformation process at panel (a2), and the red curve represents the final fracture process. (b) Elastic strain induced by the compress-to-bend test.⁴¹ (b1) A series of representative images of a diamond nanoneedle in a fully reversible elastic deformation process. (b2) FEM simulation result to reproduce the maximum bending of needle in panel (b1), showing the maximum tensile strain (10.1%) in the red text and compressive strain (11.4%) in the blue text. (b3) The SAED pattern of the bent needle located in the area enclosed by the red dotted circle at panel (b1). (b4) The theoretical stress-strain curves of uniaxial tension along different crystal orientations for bulk diamond along the [100] (green line), [110] (pink line), and [111] (orange line) directions. The maximum experimental stress along these directions are marked on the curve with circles, which are 125, 84, and 82 GPa for [100], [110], and [111] directions, respectively. (c) Elastic strain induced by the uniaxial tensile test.⁴² (c1) A representative TEM image of a fabricated bridge-shaped diamond sample and a diamond gripper moving in the direction of the red arrow. (c2) A series of representative images of strained diamond stretched along the axial direction during three loading-unloading tests in the same diamond bridge sample. Three runs were carried out with tensile strains of 4.8%, 6.8%, and 7.5%, respectively. These values of elongation are measured by the length between the fiducial markers on the surface of the diamond bridge. (c3) FEM simulation result of the stretched diamond bridge to reproduce the maximum elastic deformation in panel (c2). The SAED pattern of [001] zone axis verifies that the loading at panel (c2) is along the [101] direction. (c4) Corresponding to the experimental engineering stress-engineering strain curves in panel (c2). (d) Elastically reversible deformation of amorphous carbon by a uniaxial compression test.⁴⁷ (d1) HRTEM image and SAED pattern of a 94% sp^3 -bond amorphous carbon sample; two diffraction rings in SAED pattern are about 2.1 and 1.2 Å. (d2) Plasmon energy-fraction of sp^3 curves for different carbon materials. The sp^3 fraction of the sample can be estimated by the plasmon peak position in the low loss EELS spectra. (d3) A set of typical SEM images of 94% sp^3 -bond amorphous carbon micropillar in an *in situ* loading-unloading test. The sample exhibits a fully reversible elastic deformation. (d4) Corresponding to the experimental engineering stress-engineering strain curves in panel (d3). Panel (a) is reprinted with permission from Banerjee *et al.* Science **360**, 300 (2018). Copyright 2018, The American Association for the Advancement of Science. Panel (b) is reprinted with permission from Nie *et al.* Nat. Commun. **10**, 5533 (2019). Copyright 2019; the Author(s) are licensed under a Creative Commons Attribution 4.0 International License. Panel (c) is reprinted with permission from Dang *et al.* Science **371**, 76 (2021). Copyright 2021, The American Association for the Advancement of Science. Panel (d) is reprinted with permission from Zhang *et al.* Natl. Sci. Rev. **9**, nwab140 (2021). Copyright 2021; the Author(s) 2021, Copyright 2025 China Science Publishing & Media Ltd.

sp^3 -bonded sample were shown in Fig. 1(d1), implying a typical amorphous structure of the sample. Using plasmon peak position in low-loss electron energy loss spectroscopy (EELS), the maximum fraction of sp^3 in a series of amorphous carbon samples was estimated at ~94%, approaching diamond of 100%, as shown in Fig. 1(d2). The amorphous carbon with the highest fraction of sp^3 was experimented with an *in situ* compressive test to investigate its compressive strength. As shown in Fig. 1(d3), the 94% sp^3 -bond amorphous carbon micropillar exhibited a fully elastically reversible deformation in the loading–unloading process, and fracture was not found after unloading. According to the engineering stress–strain curve, the compressive strength of ~94% sp^3 -bond amorphous carbon was estimated at least 40 GPa, as shown in Fig. 1(d4). The study of dynamic strain of diamond established the strength theory and deformation mechanism of microfabricated diamond, revealing extreme elastic strain of diamond.

III. STATIC STRAIN IN DIAMOND

Although elastic strain is generated in diamond through *in situ* mechanical tests in SEM/TEM, the strain will disappear after unloading. Carrying out static strain in diamonds without requiring external loading has been challenging due to the ultrahigh hardness and brittleness of diamond. The current experimental strategies for inducing static strain into diamond include ion implantation, coating, and heteroepitaxy, as shown in Fig. 2(a).

Ion implantation potentially functions as a strategy for inducing static strain on diamond. Strain can occur and be fixed locally due to the mismatch between the carbon atoms in the diamond and the external atoms from implantation, such as boron (B),^{48,49} xenon (Xe),^{50,51} and helium (He).^{52,53} Ion implantation is a mature process technology and occupies an important position in silicon-based semiconductor device fabrication.⁵⁴ Ions are generated in an ions source, accelerated by a high-energy electric field, and thereafter precisely directed to introduce into the substrate.⁵⁵ The energy of the accelerated ions and the dose rate of ion implantation play crucial roles in tuning the implantation depth and ion concentration, respectively.⁵⁶ During the process of ion implantation, strain can be introduced into the target substrate, such as in tungsten and gallium nitride.^{57–59} Diamond also can be imparted with a strain by implantation of helium ions.⁶⁰ A schematic illustration of the ion implantation into diamond is shown in Fig. 2(b1). Helium ions were accelerated and bombarded into a monocrystal $\langle 100 \rangle$ diamond plate and detected by the ion counter. A molybdenum (Mo) plate was used to grip and heat the diamond by means of a thermocouple. In this experiment, the implanted $^4\text{He}^+$ ions had an energy of 275 keV and a dose of 6.4×10^{16} ions cm^{-2} at 1573 K. Under TEM characterization at a higher magnification, two-dimensional helium plates were found to present a parallel distribution, as shown by yellow arrows in Fig. 2(b2). Using electron diffraction, the pattern revealed the streaks of slim disk-shaped helium platelets, as shown in the inset of Fig. 2(b2). Using the first-principle DFT calculations, geometric matching between helium atoms and the surrounding diamond lattice was calculated, and an atomic structure model of two-dimensional solid helium was proposed. The lattice constants along the a, b, and c axes of the 2D solid helium were 2.52, 2.52, and 14.25 Å, respectively, as shown in Fig. 2(b4). Using the STEM strain mapping, 2D solid helium

can induce substantial elastic strain within the diamond lattice, as shown in Fig. 2(b5). Notably, the strain was considerably induced in the normal direction, reaching ~10% compressive and tensile strain, which can potentially function as a controllable directional elastic strain doping for applications of strain-induced diamond devices.

Moreover, coating thin film stressor also acts as a potential method of introducing static elastic strain in diamond. The thin film is deposited on the diamond substrate under heating and shrinks after cooling. Due to the difference in thermal expansion coefficient between the thin film material and diamond, the shrinkage of these materials differs, leading to a residue strain in the diamond. For example, the thermal expansion coefficient of a diamond of $\sim 1.057 \times 10^{-6} \text{ K}^{-1}$ at room temperature is smaller⁶¹ compared to that of silicon nitride (SiN) of $\sim 1.3\text{--}1.7 \times 10^{-6} \text{ K}^{-1}$,⁶² resulting in a stretch-induced static strain of diamond after cooling. For silicon, using the SiN thin film stressor, strained silicon exhibits a significant linear electro-optic effect, offering a novel structure of silicon-based optical modulator.⁶³ For diamond, the SiN thin film also acts as a stressor to induce static strain.⁶⁴ As shown in Fig. 2(c1), a series of freestanding diamond cantilever beams were microfabricated using ion beam etching and a 60 nm SiN thin film was deposited on the cantilever beams' surface using plasma enhanced chemical vapor deposition (PECVD). Prominent bending was observed on the diamond cantilever beams under the SiN thin film stretching. The bending-induced strain enlarged the ground state splitting (Δ_{GSS}) of the silicon-vacancy center embedded into the diamond cantilever, which can be characterized using photoluminescence (PL), as shown in Fig. 2(c2). Under the strain, Δ_{GSS} can be increased from ~200 to ~600 GHz upon SiN depositing, proving the fixing of strain. Using FEM simulation to reproduce the bent SiN-deposited diamond cantilever in Fig. 2(c1), a typical strain distribution of a pure bent cantilever beam is shown in Fig. 2(c3). The strain component parallel (ϵ_{yy}) and vertical (ϵ_{xx}) in-plane relative to the beam were uniformly distributed along the axial direction of the beam, exhibiting a significant depth correlation. Especially, ϵ_{yy} demonstrated a gradient distribution in the bending direction, offering a potential approach for fixing static strain in a diamond cantilever beam.

In addition, static strain can also be introduced and maintained during the growth of a heteroepitaxy film due to lattice mismatch at the heterointerface.^{65,66} For example, a static strain of ~1% was introduced in the silicon through silicon/silicon germanium (SiGe) multilayer structures, which was an efficient strategy to enhance carrier mobility.⁶⁷ In addition, heteroepitaxial germanium on a silicon substrate can be converted from indirect to direct bandgap under strain conditions.⁶⁸ Furthermore, strain can be *in situ* controlled in heteroepitaxy of silicon carbide (SiC) by changing the carbon to silicon ratio of growth.⁶⁹ Although strain is experimentally introduced into semiconductor materials through adding a heteroepitaxy film, carrying out the same method into diamond encounters challenges due to significant lattice mismatch between diamond and substrate materials. Cubic boron nitride (cBN) is a material composed of boron and nitrogen with a diamond cubic structure, exhibiting properties similar to diamond, such as superhigh hardness, low thermal expansion coefficient, and short bond length. Currently, deformation twinning was observed in a $\langle 100 \rangle$ -oriented cBN pillar, which is a continuous-transition mechanism similar to that of diamond.⁷⁰ Notably, the lattice mismatch between diamond (lattice constant of

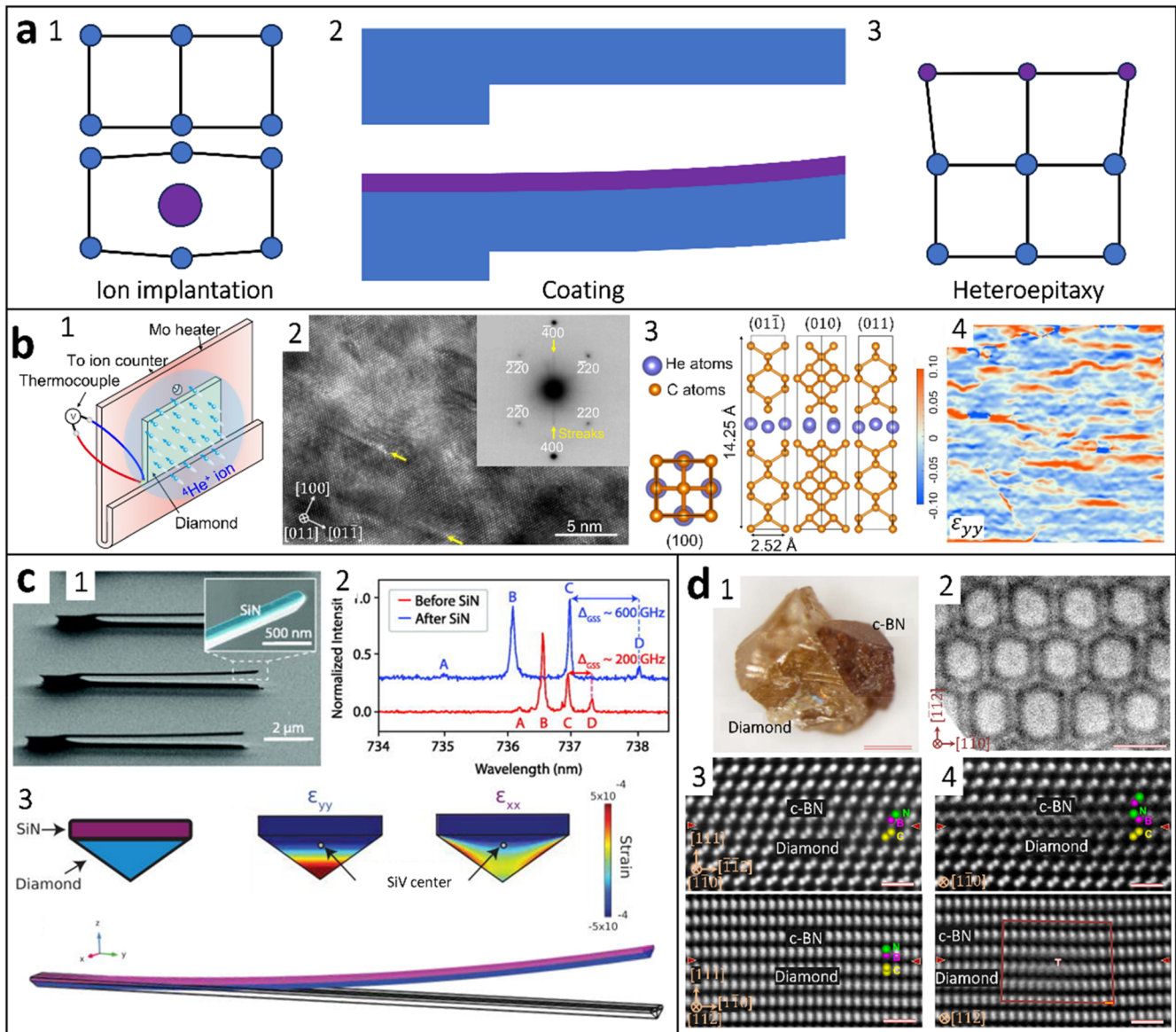


FIG. 2. Static strain in diamond. (a) Various experimental methods to inducing static strain into diamond.⁶⁰ (b) $^4\text{He}^+$ ion implantation into diamond.⁶⁰ (b1) The schematic illustration of ion implantation into diamond. Diamond is heated and bombarded with $^4\text{He}^+$ ions. (b2) High-magnification TEM image and SAED pattern (inset) show a two-dimensional helium plates region, which are pointed out by the yellow arrows. (b3) Atom arrangement of carbon and implanted He using DFT simulation. (b4) STEM perpendicular normal (ϵ_{yy}) strain mapping of implantation region in doped diamond. (c) Coating thin film stressor on the surface of diamond.⁶⁴ (c1) SEM images of a series of freestanding SiN-coated diamond cantilever beams. (c2) Photoluminescence (PL) spectra of SiV in the diamond cantilever beam at 4 K before (red) and after (blue) coating of SiN. Optical transitions are shifted and ground state splitting Δ_{GSS} is increased under the strained SiN film. (c3) FEM simulation result to reproduce bent deformation of the SiN-coated diamond cantilever beam. (d) cBN heteroepitaxy on diamond.⁷² (d1) An optical image of the heteroepitaxial cBN on diamond using the HPTH method. (d2) A bright-field TEM image of the heterointerface of the diamond–cBN sample taken along the $[111]$ zone axis. (d3) Annular dark-field (HAADF) scanning TEM (STEM) images of the coherent region of cBN–diamond heterointerface along $[110]$ and $[112]$ zone axes. (d4) HAADF-STEM images of regions containing stacking fault and Shockley partial dislocation along $[110]$ and $[112]$ zone axes. Panel (b) is reprinted with permission from Lin *et al.* Nat. Commun. **13**, 5990 (2022). Copyright 2022; the Author(s) are licensed under a Creative Commons Attribution 4.0 International License. Panel (c) is reprinted with permission from Assumpcao *et al.* Appl. Phys. Lett. **123**, 244001 (2023). Copyright 2023, AIP Publishing LLC. Panel (d) is reprinted with permission from Chen *et al.* Nat. Commun. **6**, 6327 (2015). Copyright 2015; the Author(s) are licensed under a Creative Commons Attribution 4.0 International License.

$\sim 3.567 \text{ \AA}$) and cBN (lattice constant of $\sim 3.615 \text{ \AA}$) is significantly small ($\sim 1.4\%$); therefore, cBN is considered an ideal heteroepitaxy film material to induce static strain in diamond.⁷¹ Using the HPHT method, a bulk cBN was grown on the diamond surface, with a size of $\sim 0.5 \text{ mm}$, as shown in Fig. 2(d1).⁷² A bright-field TEM image of the heterointerface of the FIB-fabricated diamond-cBN sample was taken along the $[111]$ zone axis, as shown in Fig. 2(d2). Due to the lattice mismatch, a dislocation network was found to consist of periodically arranged hexagonal dislocations. The hexagonal loops were composed of full edge dislocations with a Burgers vector of $1/2\langle 1\bar{1}0 \rangle$ and a dislocation line of $\langle 11\bar{2} \rangle$. The $1/2\langle 1\bar{1}0 \rangle$ dislocation can be dissociated into two $60^\circ 1/6\langle 1\bar{2}1 \rangle$ Shockley partial dislocations, which were connected by a $\sim 5 \text{ nm}$ stacking fault region. The sum energy of two $60^\circ 1/6\langle 1\bar{2}1 \rangle$ dislocations and a stacking fault was lower than a $1/2\langle 1\bar{1}0 \rangle$ dislocation in (111) interface, indicating that the periodical dislocation loop, composed of continuous misfit dislocations and stacking faults, was energetically preferred. Using annular dark-field (HAADF) scanning TEM (STEM), an atomically smooth heterointerface of diamond-cBN along $[1\bar{1}0]$ and $[11\bar{2}]$ zone axes in the coherent region indicated the nearly perfect cBN heteroepitaxy on the diamond, as shown in Fig. 2(d3). A representative stacking fault occurred on the side of cBN along the $[1\bar{1}0]$ zone axis, implying that the hardness of cBN is lower than that of diamond. A typical Shockley partial dislocation can be found on the side of the diamond along the $[11\bar{2}]$ zone axis, indicating the smaller lattice of the diamond, as shown in Fig. 2(d4). The crystal mismatch-induced periodical dislocation network exhibited a novel mechanism for misfit accommodation between diamond and cBN.

Fixing static strain on diamond will be a pivotal strategy to realize the preparation of strained diamond devices, keeping the strain-modulated electronic properties in the use of the devices. Ion implantation can introduce large-scale static strain in the implantation layer, while irradiation damage is generated along the implantation directions. Ion implantation also has requirements for equipment, as it is capable of generating high-energy ion beams. Heteroepitaxy has potential for creating uniform static strain in diamond, controlling the level of strain by lattice mismatch of the substrate. Since diamond is synthesized under high temperature ($\sim 1000^\circ\text{C}$), substrate material still lacks an appropriate option. These materials face challenges related to mismatches in lattice constants, melting points, and thermal expansion coefficients, which is also a crucial hindrance from wafer-sized single crystal diamond. Coating may be an effective strategy for introducing static strain in diamond, which features controllability and adaptability to micro-nano fabrication. Nevertheless, the magnitude of strain is limited to a low range, typically less than 1% , which may be restricted by factors such as the hardness of the coating, Young's modulus, and the interfacial bonding strength.

IV. MODULATING OF THERMAL, ELECTRICAL, AND QUANTUM PROPERTIES OF DIAMOND BY STRAIN ENGINEERING

As an ultrawide bandgap material, the 5.47 eV bandgap enables diamond to withstand high voltage of $\sim 10 \text{ kV}$ and has wide potential applications in high-power electronics.⁷³ Nonetheless, the sluggish progress in diamond semiconductor development is attributed to

the challenge of efficient n-type doping.^{74,75} Strain engineering provides a novel strategy to accelerate the realization of diamond semiconductors.

Strain can increase or decrease atomic distance and, therefore, change the volume or break symmetry of a material. By applying strain, bonding states and charge distribution can be changed, thereby enabling the modulation of the electrical properties of materials.⁷⁶ For example, ultrahigh pressure of 400 GPa can compress diamond and bring plastic deformation, and first-principle calculations predicted a bandgap increase from 5.3 to 6.5 eV , as shown in the density of states in Fig. 3(a).⁷⁷ Tensile strain, on the other hand, is believed to decrease the bandgap of single-crystal diamond. After having achieved ultralarge strain on nanoscale diamond experimentally,³⁹ Dang *et al.* investigated in first-principle calculations and predicted that when diamond was stretched along the $[100]$, $[101]$, or $[111]$ directions, the bandgap of diamond was reduced, by up to 2.5 eV , as shown in Fig. 3(b).¹³ Such a reduction of bandgap was preliminarily confirmed in their experimental work where electron energy-loss spectroscopy was employed. In addition to the bandgap reduction, a transition from indirect to direct bandgap was observed when more than 9% tensile strain was applied at the $[111]$ direction, opening up potential applications in optoelectronic applications such as light-emitting diodes and laser diodes.⁷⁸ Since diamond can be fabricated into patterned nanostructures, which can be further stretched uniformly, this strategy provided a way to modulate the electrical properties of diamond, making it suitable for application in practical devices.

Following the work of achieving ultralarge strain in nanoscale diamond, a series of works was published to further investigate the effects of strain to the electrical properties of diamond. While tensile strain was believed to reduce the bandgap of diamond, machine learning was employed to find out the most energy-efficient strain pathway to realize this.³³ In addition to applying uniaxial stress, complex strains can be employed to modulate the electrical properties of diamond more efficiently and more fundamentally. For example, by applying shear and compressive strains together, diamond showed a metallic property such that a bandgap closure was observed, as shown in Fig. 3(c).⁷⁹ In this case, compressive strain prevented the cleavage-type graphitization of diamond while the shear strain induced a smooth plastic flow and electronic conduction in a diamond crystal. To further increase the compression-shear strain, electronic states accumulated near the Fermi energy and superconductivity occurred when strain reached 0.349 , as shown in Fig. 3(e), predicting a transition of diamond from semiconducting to conducting and even superconducting states.⁸⁰ In addition to the modulation of bandgap, strain engineering can also tune the carrier mobility. For example, 2% shear strain along the $[100]$ direction suppressed the electron-phonon scattering of diamond, therefore, increasing the hole mobility by 800% .⁸¹ Through strain engineering, diamond exhibits a wide range of tunable electrical properties, thereby expanding its potential for diverse technological applications.

Strain engineering can tune the electrical properties of not only pure diamond but also doped diamond. It is well known that nitrogen-doped diamond takes the C_{3v} symmetry and shows a deep donor state.⁸² Such a deep-donor level corresponds to extremely high activation energy, which is hardly usable for room-temperature electronics. Simulation work predicted that with the presence of

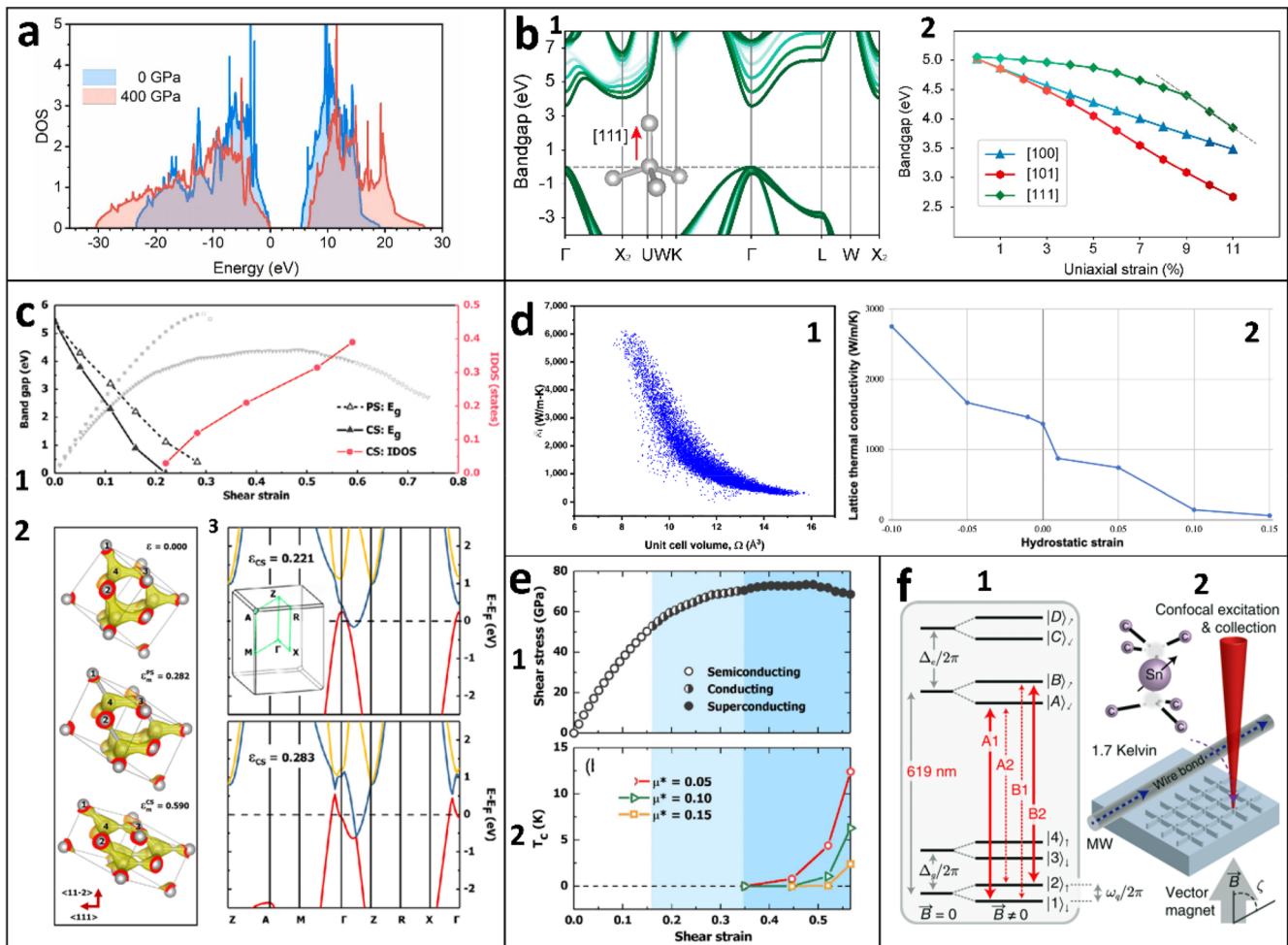


FIG. 3. Modulating of thermal, electrical, and quantum properties of diamond by strain engineering. (a) Comparison of total density of states of diamond at hydrostatic pressures of 0 and 400 GPa;⁷⁷ (b) under the uniaxial tension condition, (1) evolution of diamond band structure at tensile strain along [111] direction and (2) summary of bandgap reduction along the [100], [101], and [111] directions;⁴² (c) (1) bandgap of deformed diamond along pure shear (PS) strain and compression constrained shear (CS) strain conditions, (2) crystal structure with valence charge density, and (3) band structures shows bandgap closure;⁷⁹ (d) thermal conductivity of diamond modulated by hydrostatic strain;⁸³ (e) electrical behaviors of diamond modulated from semiconducting to conducting, and superconducting by CS strain;⁸⁰ and (f) under tensile strain condition, (1) energy diagram of negatively charged SnV center and (2) the qubit controlled by microwave (MW) pulses.⁸⁵ Panel (a) is reprinted with permission from Guo *et al.* *Extreme Mech. Lett.* **66**, 102113 (2024) Copyright 2023 Elsevier Ltd. Panel (b) is reprinted with permission from Dang *et al.* *Science* **371**, 76 (2021). Copyright 2021, The American Association for the Advancement of Science. Panel (c) is reprinted with permission from Liu *et al.* *Phys. Rev. Lett.* **123**, 195504 (2019). Copyright 2019 by the American Physical Society. Panel (d) is reprinted with permission from Shi *et al.* *Proc. Natl. Acad. Sci. U.S.A.* **121**, e2313840121 (2024). Copyright 2024; the Author(s) are licensed under a Creative Commons Attribution-NonCommercial-NoDerivatives License 4.0. Panel (e) is reprinted with permission from Liu *et al.* *Phys. Rev. Lett.* **124**, 147001 (2020). Copyright 2020 by the American Physical Society. Panel (f) is reprinted with permission from Rosenthal *et al.* *Phys. Rev. X* **13**, 031022 (2023). Copyright 2023; the Author(s) are licensed under a Creative Commons Attribution 4.0 International License.

compressive strain, especially compressive strain (>9%) along the [100] direction, the local symmetry of nitrogen-doped diamond evolved from C_{3v} toward T_d , along with spin degeneracy and the donor level shifted from a deep to shallow state.³⁰ Considering the difficulty in preparing effective n-type diamond at room temperature via conventional doping, strain engineering could be employed together with doping to modulate the semiconducting properties of the doped diamond.

In addition to the modulation of electrical properties, strain engineering can also modulate the thermal and quantum properties of diamond. Thermal conductivity exhibits an inverse correlation with the unit cell volume, demonstrating that compressive strain-induced reduction in unit cell dimensions leads to enhanced thermal conductivity, while volume expansion results in decreased thermal conductivity. Based on this principle, thermal conductivity of diamond can be doubled to over $5000 \text{ W m}^{-1} \text{ K}^{-1}$ or decreased to

below $100 \text{ W m}^{-1} \text{ K}^{-1}$, which can be seen in Fig. 3(d).⁸³ This allows diamond to be applied in more high-power scenarios with tough thermal-management requirements. Since strain changes the atomic distance and interaction of atomic orbitals, quantum mechanical properties of the diamond color center may be changed. In addition, strain changes the symmetry of diamond and enables more spin manipulation. As a result, the quantum mechanical properties of diamond can be manipulated. Therefore, strain engineering is a promising method to modulate the quantum mechanical properties of diamond, with color centers such as NV, SiV, GeV, and SnV involved in this topic.⁸⁴ For instance, tensile strain can suppress the electron-phonon interaction of SnV center (especially at high temperatures) and enhance coherence, as shown in Fig. 3(f).⁸⁵

V. APPLICATIONS IN SENSORS AND QUANTUM TECHNOLOGIES

For several decades, diamond was limited to applications in mechanical areas such as cutting, polishing, and stamping.^{86,87} Currently, hexagonal diamond was synthesized and exhibited hardness of 155 GPa.⁸⁸ However, a land-standing gap has not been covered between its excellent functional properties beyond hardness and novel applications in sensing and quantum technology. As an appealing strategy, strain engineering establishes a bridge from theoretically excellent performance to practical application for diamond-based devices.

The unavailability of scalable manufacturing has hindered the development of diamond-based electronic applications, especially for large-sized diamond films with superhigh flexibility and ultralow surface roughness. In 2024, a method capable of large-scale production of ultraflat and superflexible freestanding diamond films was developed, overcoming the bottleneck in manufacturing high-quality diamond films.⁸⁹ The diamond film was grown on a single silicon substrate using the microwave plasma chemical vapor deposition (MPCVD) method, with thickness ranging from 200 to 800 nm. The as-grown diamond surface, characterized by atomic force microscopy (AFM), exhibited a roughness of $\sim 36 \text{ nm}$. The secret of ultralow roughness was on the buried surface, that is, the side of the diamond film close to the silicon substrate after exfoliation, with an outstanding value of $\sim 0.612 \text{ nm}$. The ultrasmooth surface with a comparable size of the silicon wafer ($\sim 2 \text{ in.}$) was obtained by mechanical exfoliation without any polishing. The exfoliated diamond film demonstrated remarkable flexibility due to its reduced thickness and is able to withstand standard lithography processes, as evidenced by the successful fabrication of a diamond film with a strain sensors array, as shown in Fig. 4(a1). The 5×3 array of strain sensors was composed of Au electrodes, ultraviolet ozone-treated region, and hydrogen-terminated region of the diamond film, as shown in Fig. 4(a2). It is well-known that the skin will be compressed or stretched when muscle contraction or relaxation occurs. The strain sensor arrays of flexible diamond films can be attached to the skin, inducing strain as the skin deforms. The resistance of a diamond film can be decreased when the film is stretched as the skin is relaxed, while the increase in resistance occurs when the film is in a compressive state. The state of the skin or muscle can be detected by monitoring the change of films' resistance, indicating the potential for flexible mechanical sensing,^{90,91} as shown in Fig. 4(a3).

The manipulation of strain not only changes the resistance of diamond but also tunes the resonance frequency, which can act as a strategy for magnetic sensing. Diamond is the ideal material candidate for high quality-factor MEMS resonators owing to its ultrahigh Young's modulus.^{92,93} Galfenol (an iron-gallium alloy), a representative magnetostrictive material, exhibited the ΔE effect, which means Young's modulus of magnetostrictive materials can be altered during the magnetization process.^{94–96} Galfenol was deposited on the surface of the $160 \mu\text{m}$ diamond cantilever beam, functioning as an external magnetic field-induced stressor.⁹⁷ An on-chip diamond-based magnetic transducer was highly integrated with actuation, sensing, and signal readout functions, as shown in Fig. 4(b1). Under an external magnetic field, Young's modulus of the deposited galfenol film changed due to the ΔE effect, leading to a shift of the effective Young's modulus of galfenol-diamond cantilever. Consequently, the resonance of the galfenol film-coupled diamond cantilever was shifted and detected by the readout module, reflecting the external magnetic field, as shown in Fig. 4(b2). Furthermore, the density of magnetic flux can be characterized by coupling multiple galfenol-diamond magnetic sensors, as shown in Fig. 4(b3). In the future, an on-chip MEMS magnetic sensor composed of the galfenol film-coupled diamond cantilevers array can be developed, achieving high speed and exact mapping of magnetic fields. Owing to the outstanding thermal stability of diamond, the strain-induced diamond resonator transducers can be used to monitor magnetic field under extreme conditions, particularly in demanding applications such as vehicle engines and high-power wind turbines.⁹⁸

For quantum technologies, the color center embedded into diamond is regarded as a long-lived and robust solid-state single-spin system, which can be manipulated by electromagnetic fields.⁹⁹ Compared to typical external electromagnetic fields, strain engineering is a novel strategy to achieve the long-lived coherent oscillations and coherence time of color center spin for applications in quantum devices.¹⁰⁰ The underlying mechanisms responsible for this is strain increasing the energy splitting, raising the energy threshold of phonon absorption and suppressing decoherence due to thermal vibration of lattice.¹⁰¹ Tin-vacancy (SnV) center is a promising spin-photon interface for quantum networking devices due to its large anti-photon dephasing ability. However, the coherence of optical transitions was limited at 1.7 K .¹⁰² Using a uniform strain introduced into diamond, the SnV center's operating temperature was increased to 4 K , and the coherence lasted for more than 200 ms .¹⁰³ A schematic illustration of the strain-induced SnV center device is shown in Fig. 4(c1). The SnV centers embedded into diamond film were strained by fused silica substrate, and their spin states were controlled by the microwave from gold waveguide. Strain was introduced due to the mismatch of thermal expansion coefficient during an annealing process, as discussed in Sec. III static strain via coating on diamond. After the annealing process, the diamond film can be induced with a tensile strain in the range of 0.05% – 0.1% due to its larger thermal expansion coefficient than fused silica, as shown in Fig. 4(c2). Owing to the strain engineering, the dephasing time ($T_{2,\text{echo}}$, T_2^* , and $T_{2,\text{XY}}$) was maintained at 4 K —comparable with 1.7 K , implying that the time of spin coherence was elongated, as shown in Fig. 4(c3). Strain engineering suppresses the phonon-mediated decay and enhances the spin coherence of SnV, offering a potential approach

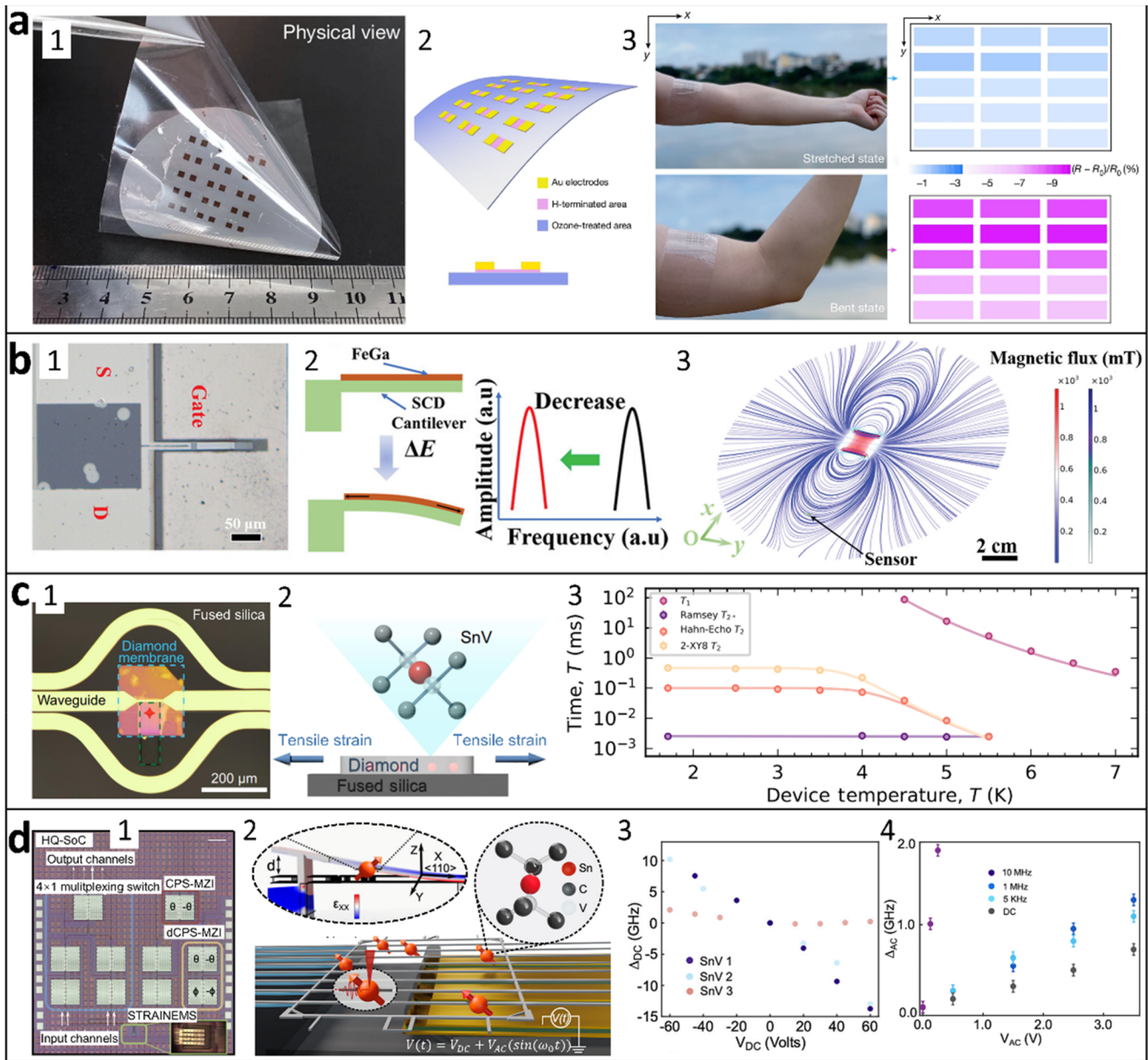


FIG. 4. Application in sensors and quantum technologies. (a) Flexible diamond films for application in a strain sensor.⁸⁹ (a1) Optical image of diamond strain sensor arrays. (a2) The schematic of strain sensor arrays using the lithography process. (a3) A strain sensor array attached to the skin to monitor the contraction or relaxation of muscle. (b) Galfenol-coupled diamond devices for application in magnetic sensing.⁹⁷ (b1) Optical image of galfenol-coupled diamond cantilever. (b2) The principle of the galfenol-coupled diamond cantilever. Under the condition of the external magnetic field, Young's modulus of the cantilever can be decreased, leading to a reduction in its resonance frequency. (b3) Simulation diagram of the magnetic sensor coupled multiple galfenol-diamond cantilever to measure magnetic flux. (c) Strain-induced SnV center device for application in solid-state quantum devices.¹⁰³ (c1) Optical image and schematic illustration of strain-induced SnV center device. (c2) The principle of strain introduction. (c3) Relaxation time (T_1^{spin} , $T_{2,\text{echo}}$, T_2^* , and $T_{2,2XY}$) as a function of temperature. Strain engineering improves spin coherence of SnV. (d) Strain-controlled quantum system on chip for application in the quantum information processor.¹⁰⁶ (d1) Optical image of the on-chip quantum system and schematic illustration of its components. (d2) The principle of STRANEMS module. Diamond cantilevers are bent upward by distance d under the piezoelectric actuators. Strain-induced SnV transition shift can be characterized by photoluminescence excitation (PLE) spectroscopy. Scatterplots of DC/AC voltage-controlled optical transition energies of SnV (Δ_{DC} , Δ_{DC}) vs DC voltage (V_{DC}) curves (d3) and AC voltage (V_{AC})(d4). Panel (a) is reprinted with permission from Jing *et al.* *Nature* **636**, 627 (2024). Copyright 2024 Springer Nature. Panel (b) is reprinted with permission from Zhang *et al.* *Adv. Funct. Mater.* **33**, 2300805 (2023). Copyright 2023 Wiley-VCH GmbH. Panel (c) is reprinted with permission from Guo *et al.* *Phys. Rev. X* **13**, 041037 (2023). Copyright 2023; the Author(s) are licensed under a Creative Commons Attribution 4.0 International License. Panel (d) is reprinted with permission from Clark *et al.* *Nano Lett.* **24**, 1316 (2024). Copyright 2024; the Author(s) are licensed under a Creative Commons Attribution-NonCommercial-NoDerivatives License 4.0.

for utilizing and developing solid-state quantum devices at higher temperature.

The mechanics of solid-state quantum optical interface is interval electronic transitions. Owing to the robust storage of quantum state in diamond, heterogeneous integration of diamond-based qubits with flying photonic qubits consistently remains in the spotlight.^{104,105} Furthermore, scalability and low power dissipation of optical routing and coherent spin control are significant challenges for quantum information processors. A strain-controlled quantum system on chip was constructed, exhibiting scalability in optical access and individual color-center control, as well as ultralow power dissipation.^{106,107} The on-chip quantum system consisted of strain-controlled SnV centers embedded into diamond arrays (the STRANEMS module), photon switches, and optical waveguide, as shown in Fig. 4(d1). The STRANEMS module had eight diamond cantilevers embedded with SnV centers. These cantilevers were strained by piezoelectric actuators at one end and optically coupled to the SiN waveguides at the other end, achieving the eight channels synchronous optical transitions of SnV centers. The strain-induced shift of SnV center transitions (Δ_c) can be characterized by photoluminescence excitation (PLE) spectroscopy, as shown in Fig. 4(d2). The strain was controllable by changing the voltage of piezoactuators owing to the piezoelectric effect. The applied voltage was divided into DC voltage (V_{DC}) and AC voltage (V_{AC}), driving the diamond cantilevers' static bending and mechanical resonances, respectively. Through changing DC voltage, the static strain-induced shift of SnV transition (Δ_{DC}) can achieve frequency modulation of over 20 GHz under superlow power dissipation (<1 nW) conditions. The strain distribution was also significantly dependent on the spatial position of the SnV center, including both the lateral position and the vertical depth, as shown in Fig. 4(d3). The energy shift of SnV transition under AC voltage-driving (Δ_{AC}) can be extended ~1.9 GHz at mechanical resonance (~10 MHz AC frequency), implying a 20-fold increase than AC frequencies (DC, 5 kHz and 1 MHz), as shown in Fig. 4(d4). This means the AC-driving mechanical resonance can be utilized to enhance the strain response of SnV centers, allowing the rapid frequency tuning of quantum memories with ultralow power consumption. Strain diamond devices may be in the form of strain coupled with multi-physical fields, providing new strategies for the fields of high-performance semiconductors and microelectronics/optoelectronic devices.

VI. CONCLUSIONS AND PERSPECTIVES

In this review, we focus on the approaches for introducing strain in microfabricated diamond, including carrying out dynamic strain by an *in situ* nanomechanical test and fixing static strain by ion implantation, coating stressor film, and heteroepitaxy. Strain engineering is an efficient and significant strategy to manipulate the properties of diamond, including bandgap, thermal conductivity, and shift of color center transition, expanding the application potential of diamond. Furthermore, strain distribution of microfabricated diamond is fully controllable by tuning the source of strain, such as magnetostriuctive film and piezoelectric actuators, which can be utilized in applications for sensing and quantum technologies.

Carrying out strain in a diamond is kept challenging due to its ultrahigh hardness and brittleness, especially introducing, controlling and maintaining a large strain. Although a small-value strain is

held in the diamond, it is far from the ultralarge strain achieved in a one-dimension diamond by *in situ* nanomechanical testing. The crucial requirements for introducing large strains in diamond are to have minimal internal defects and smooth surface. As for difficulty in achieving the fixation of large strains, the underlying reason lies in the lack of strain-fixing materials whose mechanical properties (Young's modulus, hardness etc.) are comparable with diamond. A potential solution is to use a material such as nano-twinned diamond, of which the hardness (~200 GPa) is even higher than that of diamond (~100 GPa).¹⁰⁸ The development of nanomechanical techniques, including micro/nano fabrication, ultralarge strain fixing, nanomechanical test, and devices design and fabrication, is critical to addressing these challenges. In the future, two-dimensional array diamond has potential for achieving diversity of strain applied to strain engineering design, opening up new opportunities for high-performance and low-energy-dissipation diamond-based MEMS. Moreover, diamond with a three-dimensional lattice structure functions as a metamaterial for application in optoelectronic devices, which imposes higher requirements on the micro/nanofabrication and multiphysics field coupling characterization technology.

ACKNOWLEDGMENTS

The authors acknowledge the financial support from the Research Grants Council of the Hong Kong Special Administrative Region, China under Grant Nos. RFS2021-1S05 and N_HKU159/22 and the Department of Science and Technology of Hunan Province under Grant No. 2023GK2013.

AUTHOR DECLARATIONS

Conflict of Interest

The authors have no conflicts to disclose.

Author Contributions

Wenjun Liang: Conceptualization (lead); Data curation (lead); Methodology (equal); Visualization (lead); Writing – original draft (lead); Writing – review & editing (equal). **Limin Yang:** Conceptualization (equal); Methodology (equal); Visualization (equal); Writing – original draft (equal); Writing – review & editing (equal). **Jiaqi Zhu:** Conceptualization (equal); Methodology (equal); Writing – review & editing (equal). **Yiling Lian:** Methodology (equal); Writing – review & editing (equal). **Yang Lu:** Conceptualization (equal); Funding acquisition (lead); Project administration (lead); Supervision (lead); Writing – review & editing (equal).

DATA AVAILABILITY

The data that support the findings of this study are available from the corresponding author upon reasonable request.

REFERENCES

- M. Schreck, S. Gsell, R. Brescia, and M. Fischer, *Sci. Rep.* **7**(1), 44462 (2017).
- X. Guo, M. Xie, A. Addhya, A. Linder, U. Zvi, S. Wang, X. Yu, T. D. Deshmukh, Y. Liu, I. N. Hammock, Z. Li, C. T. DeVault, A. Butcher, A. P. Esser-Kahn, D. D. Awschalom, N. Deegan, P. C. Maurer, F. J. Heremans, and A. A. High, *Nat. Commun.* **15**(1), 8788 (2024).

- ³Y. Tao, J. M. Boss, B. A. Moores, and C. L. Degen, *Nat. Commun.* **5**(1), 3638 (2014).
- ⁴M. H  ritier, A. Eichler, Y. Pan, U. Grob, I. Shorubalko, M. D. Krass, Y. Tao, and C. L. Degen, *Nano Lett.* **18**(3), 1814 (2018).
- ⁵A. Toros, M. Kiss, T. Graziosi, H. Sattari, P. Gallo, and N. Quack, *Microsyst. Nanoeng.* **4**(1), 12 (2018).
- ⁶H. J. Wang, D. W. Zuo, F. Xu, and W. Z. Lu, *Mater. Trans.* **58**(1), 91 (2017).
- ⁷B. Khanaliloo, M. Mitchell, A. C. Hryciw, and P. E. Barclay, *Nano Lett.* **15**(8), 5131 (2015).
- ⁸T. Graziosi, S. Mi, M. Kiss, and N. Quack, *APL Photonics* **3**(12), 126101 (2018).
- ⁹J. J. Bernstein, M. G. Bancu, J. M. Bauer, E. H. Cook, P. Kumar, E. Newton, T. Nyinjee, G. E. Perlin, J. A. Ricker, W. A. Teynor, and M. S. Weinberg, *J. Manuf. Syst.* **25**(8), 085006 (2015).
- ¹⁰A. Heidari, M. L. Chan, H. A. Yang, G. Jaramillo, P. Taheri-Tehrani, P. Fonda, H. Najar, K. Yamazaki, L. Lin, and D. A. Horsley, in Presented at the 2013 Transducers & Eurosensors XXVII: The 17th International Conference on Solid-State Sensors, Actuators and Microsystems (TRANSDUCERS & EUROSensors XXVII), 2013.
- ¹¹Y. Sasama, T. Kageura, M. Imura, K. Watanabe, T. Taniguchi, T. Uchihashi, and Y. Takahide, *Nat. Electron.* **5**(1), 37 (2021).
- ¹²J. Su, W. Wang, G. Shao, G. Chen, and H.-X. Wang, *Appl. Phys. Lett.* **123**(17), 172105 (2023).
- ¹³Y. Sasama, K. Komatsu, S. Moriyama, M. Imura, T. Teraji, K. Watanabe, T. Taniguchi, T. Uchihashi, and Y. Takahide, *APL Mater.* **6**(11), 111105 (2018).
- ¹⁴N. C. Saha, S. W. Kim, K. Koyama, T. Oishi, and M. Kasu, *IEEE Electron Device Lett.* **44**(1), 112 (2023).
- ¹⁵N. C. Saha, T. Shiratsuchi, S. W. Kim, K. Koyama, T. Oishi, and M. Kasu, *IEEE Electron Device Lett.* **44**(5), 793 (2023).
- ¹⁶J. Zhang, N. Liu, L. Chen, X. Yang, H. Guo, Z. Wang, M.-Q. Yuan, X.-J. Yan, J. Yang, X. Li, C. Shan, J. Ye, and W. Zhang, *Nano Lett.* **25**(1), 537 (2025).
- ¹⁷R. Kagawa, Z. Cheng, K. Kawamura, Y. Ohno, C. Moriyama, Y. Sakaida, S. Ouchi, H. Uratani, K. Inoue, Y. Nagai, N. Shigekawa, and J. Liang, *Small* **20**(13), 2305574 (2024).
- ¹⁸J. Liang, A. Kobayashi, Y. Shimizu, Y. Ohno, S.-W. Kim, K. Koyama, M. Kasu, Y. Nagai, and N. Shigekawa, *Adv. Mater.* **33**(43), 2104564 (2021).
- ¹⁹Z. Li, W. Liang, J. Chen, L. Song, T. Xiong, W. Xie, S. Wu, D. Hu, X. Yao, and Z. Peng, *Nano Energy* **110**, 108370 (2023).
- ²⁰X.-B. Cheng, M.-Q. Zhao, C. Chen, A. Pentecost, K. Maleski, T. Mathis, X.-Q. Zhang, Q. Zhang, J. Jiang, and Y. Gogotsi, *Nat. Commun.* **8**(1), 336 (2017).
- ²¹J. Li, Z. Shan, and E. Ma, *MRS Bull.* **39**(2), 108 (2014).
- ²²C. Chien-Hao, T. L. Lee, T. H. Hou, C. L. Chen, C. C. Chen, J. W. Hsu, K. L. Cheng, Y. H. Chiu, H. J. Tao, Y. Jin, C. H. Diaz, S. C. Chen, and M. S. Liang, in Presented at the Digest of Technical Papers. 2004 Symposium on VLSI Technology, 2004.
- ²³L. Yang, S. Yue, T. Yi, S. Qiao, H. Li, Z. Dai, B. Song, Y. Chen, J. Du, D. Li, and P. Gao, *Nature* **629**(8014), 1021 (2024).
- ²⁴A. Beccari, D. A. Visani, S. A. Fedorov, M. J. Bereyhi, V. Boureau, N. J. Engelsens, and T. J. Kippenberg, *Nat. Phys.* **18**(4), 436 (2022).
- ²⁵S. Belarouci, T. Ouahrani, N. Benabdallah,   . Morales-Garc  a, and I. Belabbas, *Comput. Mater. Sci.* **151**, 288 (2018).
- ²⁶L. Zhou, T. Yang, L. Zhu, W. Li, S. Wang, X. Hou, X. Mao, and Z. L. Wang, *Nano Energy* **83**, 105826 (2021).
- ²⁷M. Minary-Jolandan, R. A. Bernal, I. Kuljanishvili, V. Parpoil, and H. D. Espinosa, *Nano Lett.* **12**(2), 970 (2012).
- ²⁸Z. Shi, M. Dao, E. Tsymbalov, A. Shapeev, J. Li, and S. Suresh, *Proc. Natl. Acad. Sci. U. S. A.* **117**(40), 24634 (2020).
- ²⁹B. Wang, Y. He, N. Rodionov, and J. Zhu, *Mater. Today Phys.* **36**, 101182 (2023).
- ³⁰L. Yang, R. Fan, A. Hu, J. Ma, Y. Liu, and Y. Lu, *Appl. Phys. Lett.* **123**(6), 062105 (2023).
- ³¹A. Lu, L. Yang, C. Dang, H. Wang, Y. Zhang, X. Li, H. Zhang, and Y. Lu, *Funct. Diamond* **2**, 151 (2022).
- ³²D. Y. Liu, L. C. Hao, Y. Teng, F. Qin, Y. Shen, K. Tang, J. D. Ye, S. M. Zhu, R. Zhang, Y. D. Zheng, and S. L. Gu, *APL Mater.* **9**(8), 081106 (2021).
- ³³Z. Shi, E. Tsymbalov, M. Dao, S. Suresh, A. Shapeev, and J. Li, *Proc. Natl. Acad. Sci. U. S. A.* **116**(10), 4117 (2019).
- ³⁴X. Li, K. Maute, M. L. Dunn, and R. Yang, *Phys. Rev. B* **81**(24), 245318 (2010).
- ³⁵J. Xiang, H. Wang, J. Zhou, and Y. Lu, *Acta Mech. Solida Sin.* **38**, 240 (2025).
- ³⁶Y. Han, J. Zhou, H. Wang, L. Gao, S. Feng, K. Cao, Z. Xu, and Y. Lu, *Appl. Nanosci.* **11**(4), 1075 (2021).
- ³⁷Y. Han, L. Gao, J. Zhou, Y. Hou, Y. Jia, K. Cao, K. Duan, and Y. Lu, *ACS Appl. Mater. Interfaces* **14**(7), 8655 (2022).
- ³⁸C. Dang, A. Lu, H. Wang, L. Yang, X. Li, H. Zhang, and Y. Lu, *Extreme Mech. Lett.* **58**, 101931 (2023).
- ³⁹A. Banerjee, D. Bernoulli, H. Zhang, M.-F. Yuen, J. Liu, J. Dong, F. Ding, J. Lu, M. Dao, W. Zhang, Y. Lu, and S. Suresh, *Science* **360**, 300 (2018).
- ⁴⁰X. Yan, Y. Jiang, B. Yang, S. Ma, T. Yao, A. Tao, C. Chen, X. Ma, and H. Ye, *Carbon* **200**, 483 (2022).
- ⁴¹A. Nie, Y. Bu, P. Li, Y. Zhang, T. Jin, J. Liu, Z. Su, Y. Wang, J. He, Z. Liu, H. Wang, Y. Tian, and W. Yang, *Nat. Commun.* **10**, 5533 (2019).
- ⁴²C. Dang, J.-P. Chou, B. Dai, C.-T. Chou, Y. Yang, R. Fan, W. Lin, F. Meng, A. Hu, J. Zhu, J. Han, A. M. Minor, J. Li, and Y. Lu, *Science* **371**, 76 (2021).
- ⁴³K. Cao, S. Feng, Y. Han, L. Gao, T. Hue Ly, Z. Xu, and Y. Lu, *Nat. Commun.* **11**(1), 284 (2020).
- ⁴⁴J. Zhou, M. Zhu, Y. Han, X. Zhou, S. Wang, J. Chen, H. Wu, Y. Hou, and Y. Lu, *J. Appl. Phys.* **135**(22), 224301 (2024).
- ⁴⁵J. M. Wheeler, R. Raghavan, J. Wehrs, Y. Zhang, R. Erni, and J. Michler, *Nano Lett.* **16**(1), 812 (2016).
- ⁴⁶Z. Zeng, L. Yang, Q. Zeng, H. Lou, H. Sheng, J. Wen, D. J. Miller, Y. Meng, W. Yang, W. L. Mao, and H.-k. Mao, *Nat. Commun.* **8**(1), 322 (2017).
- ⁴⁷S. Zhang, Z. Li, K. Luo, J. He, Y. Gao, A. V. Soldatov, V. Benavides, K. Shi, A. Nie, B. Zhang, W. Hu, M. Ma, Y. Liu, B. Wen, G. Gao, B. Liu, Y. Zhang, Y. Shu, D. Yu, X.-F. Zhou, Z. Zhao, B. Xu, L. Su, G. Yang, O. P. Chernogorova, and Y. Tian, *Natl. Sci. Rev.* **9**(1), nwab140 (2022).
- ⁴⁸R. J. Jim  nez-Riob  o, N. Gordillo, A. de Andr  s, A. Redondo-Cubero, M. Moratalla, M. A. Ramos, and M. D. Ynsa, *Carbon* **208**, 421 (2023).
- ⁴⁹Y. Seki, Y. Hoshino, and J. Nakata, *J. Appl. Phys.* **129**(19), 195702 (2021).
- ⁵⁰J. Xu, Y. Liu, Z. Guo, W. Liang, S. Wu, J. Lin, J. Nian, D. Guo, and X. Wang, *Diamond Relat. Mater.* **133**, 109718 (2023).
- ⁵¹J. Yu, Y. Liu, J. Xu, W. Liang, W. Yue, S. Wu, Y. Yang, J. Lin, J. Nian, D. Guo, and X. Wang, *Wear* **518–519**, 204646 (2023).
- ⁵²M. Chen, J. P. Best, I. Shorubalko, J. Michler, R. Spolenak, and J. M. Wheeler, *Carbon* **158**, 337 (2020).
- ⁵³B. A. Fairchild, S. Rubanov, D. W. M. Lau, M. Robinson, I. Suarez-Martinez, N. Marks, A. D. Greentree, D. McCulloch, and S. Prawer, *Adv. Mater.* **24**(15), 2024 (2012).
- ⁵⁴R. G. Elliman and J. S. Williams, *Curr. Opin. Solid State Mater. Sci.* **19**(1), 49 (2015).
- ⁵⁵L. Huang, H. Wu, G. Cai, S. Wu, D. Li, T. Jiang, B. Qiao, C. Jiang, and F. Ren, *ACS Nano* **18**(4), 2578 (2024).
- ⁵⁶N. Teranishi, G. Fuse, and M. Sugitani, *Sensors* **18**(7), 2358 (2018).
- ⁵⁷N. W. Phillips, H. Yu, S. Das, D. Yang, K. Mizohata, W. Liu, R. Xu, R. J. Harder, and F. Hofmann, *Acta Mater.* **195**, 219 (2020).
- ⁵⁸S. Das, W. Liu, R. Xu, and F. Hofmann, *Mater. Des.* **160**, 1226 (2018).
- ⁵⁹P. Mendes, K. Lorenz, E. Alves, S. Schwaiger, F. Scholz, and S. Magalh  es, *Mater. Sci. Semicond. Process.* **98**, 95 (2019).
- ⁶⁰W. Lin, Y. Li, S. De Graaf, G. Wang, J. Lin, H. Zhang, S. Zhao, D. Chen, S. Liu, J. Fan, B. J. Kooi, Y. Lu, T. Yang, C. H. Yang, C. T. Liu, and J. J. Kai, *Nat. Commun.* **13**(1), 5990 (2022).
- ⁶¹P. Jacobson and S. Stoupin, *Diamond Relat. Mater.* **97**, 107469 (2019).
- ⁶²S. Habermehl, *J. Vac. Sci. Technol., A* **36**(2), 021517 (2018).
- ⁶³R. S. Jacobsen, K. N. Andersen, P. I. Borel, J. Fage-Pedersen, L. H. Frandsen, O. Hansen, M. Kristensen, A. V. Lavrinenko, G. Moulin, H. Ou, C. Peucheret, B. Zsigri, and A. Bjarklev, *Nature* **441**(7090), 199 (2006).
- ⁶⁴D. R. Assumpcao, C. Jin, M. Sutula, S. W. Ding, P. Pham, C. M. Knaut, M. K. Bhaskar, A. Panday, A. M. Day, D. Renaud, M. D. Lukin, E. Hu, B. Machiels, and M. Loncar, *Appl. Phys. Lett.* **123**(24), 244001 (2023).
- ⁶⁵K. Wei, T. Zhou, Y. Jiang, C. Sun, Y. Liu, S. Li, S. Liu, X. Fu, C. Hu, S. Tian, Y. Yang, X. Fu, N. AlMasoud, S. M. H. Qaid, M. K. Nazeeruddin, H.-Y. Hsu, W.-D. Li, J. T. Kim, R. Long, W. Zhang, J. Chen, and M. Yuan, *Nature* **638**, 949 (2025).

- ⁶⁶G. Zhou, W. Lv, H. Wang, Z. Nie, Y. Chen, Y. Li, H. Huang, W. Chen, Y. Sun, Q.-K. Xue, and Z. Chen, *Nature* **640**, 641 (2025).
- ⁶⁷G. Abstreiter, H. Brugger, T. Wolf, H. Jorke, and H. J. Herzog, *Phys. Rev. Lett.* **54**(22), 2441 (1985).
- ⁶⁸J. Michel, J. Liu, and L. C. Kimerling, *Nat. Photonics* **4**(8), 527 (2010).
- ⁶⁹B. Jazizadeh and M. Myronov, *Sci. Rep.* **14**(1), 30325 (2024).
- ⁷⁰Y. Bu, Z. Su, J. Huang, K. Tong, P. Li, C. Wang, T. Jin, S. Zhao, Z. Zhao, A. Soldatov, Y. Wang, B. Xu, Z. Liu, A. Nie, H. Wang, W. Yang, and Y. Tian, *Nat. Mater.* **24**, 361 (2025).
- ⁷¹E. Knittle, R. M. Wentzcovitch, R. Jeanloz, and M. L. Cohen, *Nature* **337**(6205), 349 (1989).
- ⁷²C. Chen, Z. Wang, T. Kato, N. Shibata, T. Taniguchi, and Y. Ikuhara, *Nat. Commun.* **6**(1), 6327 (2015).
- ⁷³S. Shikata, *Diamond Relat. Mater.* **65**, 168 (2016).
- ⁷⁴H. Yang, Y. Ma, and Y. Dai, *Funct. Diamond* **1**(1), 150 (2021).
- ⁷⁵M. Sultana, S. Karmakar, and A. Haque, *Mater. Sci. Semicond. Process.* **186**, 109024 (2025).
- ⁷⁶Y. Liu, S. Liu, J. Robertson, and Y. Guo, *Phys. Status Solidi RRL* **17**(1), 2200344 (2023).
- ⁷⁷S. Guo, Y. Duan, Z. Su, L. Wang, Y. Bu, A. Nie, H. Wang, and Y. Tian, *Extreme Mech. Lett.* **66**, 102113 (2024).
- ⁷⁸L.-D. Yuan, H.-X. Deng, S.-S. Li, S.-H. Wei, and J.-W. Luo, *Phys. Rev. B* **98**(24), 245203 (2018).
- ⁷⁹C. Liu, X. Song, Q. Li, Y. Ma, and C. Chen, *Phys. Rev. Lett.* **123**(19), 195504 (2019).
- ⁸⁰C. Liu, X. Song, Q. Li, Y. Ma, and C. Chen, *Phys. Rev. Lett.* **124**(14), 147001 (2020).
- ⁸¹J. Sun, S. Li, C. Shao, Z. Tong, M. An, Y. Yao, Y. Hu, X. Zhu, Y. Liu, R. Wang, X. Liu, and T. Frauenheim, *Appl. Phys. Rev.* **12**(1), 011408 (2025).
- ⁸²M. N. R. Ashfold, J. P. Goss, B. L. Green, P. W. May, M. E. Newton, and C. V. Peaker, *Chem. Rev.* **120**(12), 5745 (2020).
- ⁸³Z. Shi, E. Tsymbalov, W. Shi, A. Barr, Q. Li, J. Li, X.-Q. Chen, M. Dao, S. Suresh, and J. Li, *Proc. Natl. Acad. Sci. U. S. A.* **121**(8), e2313840121 (2024).
- ⁸⁴L. Yang, H. Wang, S. Yang, and Y. Lu, *Mater. Quantum Technol.* **4**(2), 023001 (2024).
- ⁸⁵E. I. Rosenthal, C. P. Anderson, H. C. Kleidermacher, A. J. Stein, H. Lee, J. Grzesik, G. Scuri, A. E. Rugar, D. Riedel, S. Aghaeimeibodi, G. H. Ahn, K. Van Gasse, and J. Vučković, *Phys. Rev. X* **13**(3), 031022 (2023).
- ⁸⁶H. Liu, Y. Yan, J. Cui, Y. Geng, T. Sun, X. Luo, and W. Zong, *Int. J. Extreme Manuf.* **6**(6), 062008 (2024).
- ⁸⁷B. Wang, Z. Zhang, J. Cui, N. Jiang, J. Lyu, G. Chen, J. Wang, Z. Liu, J. Yu, C. Lin, F. Ye, and D. Guo, *ACS Appl. Mater. Interfaces* **9**(35), 29451 (2017).
- ⁸⁸D. Chen, G. Chen, L. Lv, J. Dong, Y. Shang, X. Hou, Y. Wang, J. Shang, S. Wang, Y. Yin, R. Liu, W. Zhang, Z. Jiang, Y. He, B. He, C. Mao, S. Zhu, B. Sundqvist, B. Liu, and M. Yao, *Nat. Mater.* **24**, 513 (2025).
- ⁸⁹J. Jing, F. Sun, Z. Wang, L. Ma, Y. Luo, Z. Du, T. Zhang, Y. Wang, F. Xu, T. Zhang, C. Chen, X. Ma, Y. He, Y. Zhu, H. Sun, X. Wang, Y. Zhou, J. K. H. Tsoi, J. Wrachtrup, N. Wong, C. Li, D.-K. Ki, Q. Wang, K. H. Li, Y. Lin, and Z. Chu, *Nature* **636**(8043), 627 (2024).
- ⁹⁰S. Huang, Y. Liu, Y. Zhao, Z. Ren, and C. F. Guo, *Adv. Funct. Mater.* **29**(6), 1805924 (2019).
- ⁹¹Y. Wang, M. L. Adam, Y. Zhao, W. Zheng, L. Gao, Z. Yin, and H. Zhao, *Nano-Micro Lett.* **15**(1), 55 (2023).
- ⁹²Z. Zhao, Y. Li, W. Zhang, W. Luo, and D. Liu, *Microsyst. Nanoeng.* **11**(1), 12 (2025).
- ⁹³G. Chen, S. Koizumi, Y. Koide, and M. Liao, *Acc. Mater. Res.* **5**, 1087 (2024).
- ⁹⁴S. Datta, J. Atulasimha, C. Mudivarthi, and A. B. Flatau, *J. Magn. Magn. Mater.* **322**(15), 2135 (2010).
- ⁹⁵H. W. Chang, S. U. Jen, D. H. Tseng, R. F. Yung, C. R. Wang, W. C. Cheng, and W. C. Chang, *J. Alloys Compd.* **810**, 151873 (2019).
- ⁹⁶C. Zhou, Y. Liu, K. Chen, Z. Dai, T. Ma, Y. Wang, S. Ren, J. Deng, R. Zhang, F. Tian, Y. Zhang, H. Zeng, and S. Yang, *Sci. Rep.* **10**(1), 20055 (2020).
- ⁹⁷Z. Zhang, W. Zhao, G. Chen, M. Toda, S. Koizumi, Y. Koide, and M. Liao, *Adv. Funct. Mater.* **33**(27), 2300805 (2023).
- ⁹⁸G. Oliver, M. A. Willard, E. Brück, C. H. Chen, S. G. Sankar, and J. Ping Liu, *Adv. Mater.* **23**(7), 821 (2011).
- ⁹⁹R. Hanson, L. P. Kouwenhoven, J. R. Petta, S. Tarucha, and L. M. K. Vandersypen, *Rev. Mod. Phys.* **79**(4), 1217 (2007).
- ¹⁰⁰A. Barfuss, J. Teissier, E. Neu, A. Nunnenkamp, and P. Maletinsky, *Nat. Phys.* **11**(10), 820 (2015).
- ¹⁰¹Y.-I. Sohn, S. Meesala, B. Pingault, H. A. Atikian, J. Holzgrafe, M. Gündoğan, C. Stavarakas, M. J. Stanley, A. Sipahigil, J. Choi, M. Zhang, J. L. Pacheco, J. Abraham, E. Bielejec, M. D. Lukin, M. Atatüre, and M. Lončar, *Nat. Commun.* **9**(1), 2012 (2018).
- ¹⁰²R. Debroux, C. P. Michaels, C. M. Purser, N. Wan, M. E. Trusheim, J. Arjona Martínez, R. A. Parker, A. M. Stramma, K. C. Chen, L. de Santis, E. M. Alexeev, A. C. Ferrari, D. Englund, D. A. Gangloff, and M. Atatüre, *Phys. Rev. X* **11**(4), 041041 (2021).
- ¹⁰³X. Guo, A. M. Stramma, Z. Li, W. G. Roth, B. Huang, Y. Jin, R. A. Parker, J. Arjona Martínez, N. Shofer, C. P. Michaels, C. P. Purser, M. H. Appel, E. M. Alexeev, T. Liu, A. C. Ferrari, D. D. Awschalom, N. Deegan, B. Pingault, G. Galli, F. J. Heremans, M. Atatüre, and A. A. High, *Phys. Rev. X* **13**(4), 041037 (2023).
- ¹⁰⁴H. J. Kimble, *Nature* **453**(7198), 1023 (2008).
- ¹⁰⁵S. Wehner, D. Elkouss, and R. Hanson, *Science* **362**(6412), eaam9288 (2018).
- ¹⁰⁶G. Clark, H. Raniwala, M. Koppa, K. Chen, A. Leenheer, M. Zimmermann, M. Dong, L. Li, Y. H. Wen, D. Dominguez, M. Trusheim, G. Gilbert, M. Eichenfield, and D. Englund, *Nano Lett.* **24**(4), 1316 (2024).
- ¹⁰⁷L. Sementilli, E. Romero, and W. P. Bowen, *Adv. Funct. Mater.* **32**(3), 2105247 (2022).
- ¹⁰⁸Q. Huang, D. Yu, B. Xu, W. Hu, Y. Ma, Y. Wang, Z. Zhao, B. Wen, J. He, Z. Liu, and Y. Tian, *Nature* **510**(7504), 250 (2014).